Engineering Fracture Mechanics 295 (2024) 109789

Contents lists available at ScienceDirect

Engineering Fracture Mechanics

journal homepage: www.elsevier.com/locate/engfracmech

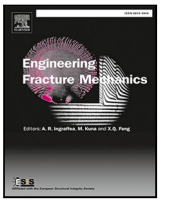

Mode I fracture analysis of Fe-SMA bonded double cantilever beam considering nonlinear behavior of the adherends

Niels Pichler [a,b,*], Wandong Wang [c,**], Masoud Motavalli [a], Andreas Taras [b], Elyas Ghafoori [d]

[a] Empa, Swiss Federal Laboratories for Materials Science and Technology, Überlandstrasse 129, 8600, Dübendorf, Switzerland
[b] Institute of Structural Engineering, Department of Civil, Environmental and Geomatic Engineering, ETH Zürich, 8093, Zürich, Switzerland
[c] School of Aeronautics, Northwestern Polytechnical University, Xi'an, Shaanxi, PR China
[d] Institute for Steel Construction, Faculty of Civil Engineering and Geodetic Science, Leibniz University Hannover, 30167 Hannover, Germany

ARTICLE INFO

Keywords:
Shape memory alloys
Steel
Debonding
Fracture mechanics
Cohesive zone modeling

ABSTRACT

In the scope of developing a bonded iron-based shape memory alloy (Fe-SMA) strengthening solution, nonlinear deformation in the adherends upon joint failure due to phase transformation and high adhesive toughness is unavoidable. The effect of this nonlinear deformation has not been studied in the case of Mode I failure. In this study, the first experimental and theoretical investigation on Mode I failure of Fe-SMA bonded joints is presented. A new analytical model is proposed and validated using experimental results to gain an in-depth understanding of the influence of Fe-SMA nonlinear material deformation on the joint failure process. The proposed model is shown to be significantly faster than traditional elasto-plastic finite elements using cohesive zone modeling with a minimum compromise to the accuracy. These are observed to result in lower bond strength and a shorter fracture process zone than that of linear elastic adherends using the same adhesive. Neglecting the nonlinear behavior of the Fe-SMA bonded joints can lead to an unconservative joint design, jeopardizing safety. The developed model is aimed at facilitating the development of adhesively bonded Fe-SMA strengthening systems.

1. Introduction

An adhesively bonded and self-prestressed fatigue strengthening solution using an *iron based shape memory alloy* (Fe-SMA), as depicted in Fig. 1, has been substantiated to be highly effective in retarding fatigue crack growth in metallic structures [1,2]. Adhesive bonding is preferred over mechanical joining for a more even stress distribution and prolonged fatigue life. In addition, the prestressing offered by the Fe-SMA material and the bridging mechanism owning to the adhesive bonding technique are synergistic in retarding the fatigue crack growth in metallic structures [1,3,4].

The Fe-SMA has been recently developed at Empa for upgrading vast deteriorating metallic infrastructures owing to increasingly severe service loads. A recovery stress of 350 MPa attributed to the *shape memory effect* (SME) of this alloy makes it highly favorable to realize a desirable compressive stress in parent structures [1]. The SME of the Fe-SMA is attributed to the phase transformation between austenite and martensite, which also results in a premature nonlinear stress–strain behavior [1,5]. Several research projects have exploited the SME of the Fe-SMA for fatigue strengthening of metallic structures [6–8]. The joining method in these research

* Corresponding author at: Empa, Swiss Federal Laboratories for Materials Science and Technology, Überlandstrasse 129, 8600, Dübendorf, Switzerland.
** Corresponding author.
E-mail addresses: niels.pichler@empa.ch (N. Pichler), w.wang@nwpu.edu.cn (W. Wang), masoud.motavalli@empa.ch (M. Motavalli), taras@ibk.baug.ethz.ch (A. Taras), ghafoori@stahl.uni-hannover.de (E. Ghafoori).

https://doi.org/10.1016/j.engfracmech.2023.109789
Received 9 August 2023; Received in revised form 10 November 2023; Accepted 6 December 2023
Available online 9 December 2023

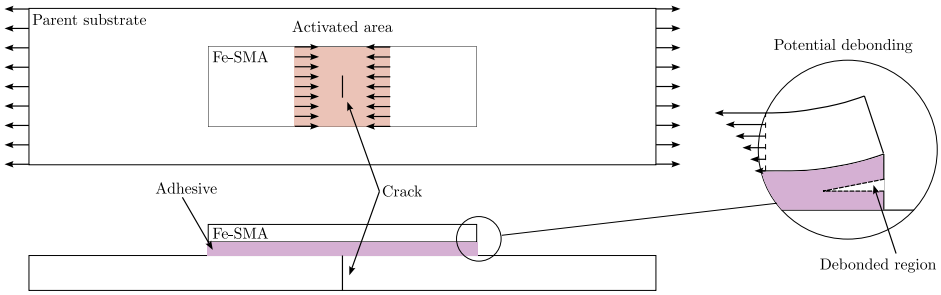

Fig. 1. Adhesively-bonded Fe-SMA patch and a potential failure in the repair system.

projects was limited to mechanical joining due to the lack of in-depth understanding of the debonding failure behavior of the adhesively bonded Fe-SMA joints.

Given the great potential of the bonded and prestressed Fe-SMA solution for fatigue strengthening of metallic structures, it is essential to study the failure behavior of the bonded Fe-SMA joints to ensure a safe design. More recent studies [9,10] have focused on Mode II failure of Fe-SMA bonded joints and shown that the Fe-SMA undergoes nonlinear material deformation and negatively affects the failure process. However, no work so far has investigated Mode I or mixed-mode failure. Yet, Fig. 1 depicts a potential mixed-mode failure initiating at the patch tip, which includes of Mode I fracture component. While mixed-mode can be considered to be the failure mode in the vast majority of application cases, it is also the most complex. To gain a better understanding of the failure of such joints, it is reasonable to continue investigations on pure Mode I fracture behavior. The importance of Fe-SMA nonlinear material behavior was established in earlier works on Mode II fracture behavior and it is therefore expected to play a role in Mode I failure of bonded Fe-SMA joints. This is the topic of the present study.

Conventional fracture analysis methods in open literature usually use beam-like specimens, such as *double cantilever beam* (DCB), *end-notched flextural* specimens (ENF) and *mixed mode bending* (MMB) to extract the fracture toughness and cohesive constitutive behavior [11]. These assume that adhesive failure is the sole energy dissipation mechanism. To accurately perform the failure analysis, no energy dissipation resulting from the nonlinear behavior of the adherends is allowed.

Solutions to prevent nonlinear material deformation in adherends during tests have been proposed, such as the use of a backing beam as a stiffener [12]. However, this method poses several problems. First of all, it needs special consideration for mode mixity [13] as well as tedious specimen preparation. Furthermore, samples can become unreasonably thick and require a significant load when tough adhesives are tested. Last but not least, circumventing the problem by avoiding nonlinear deformation in laboratory fracture tests can lead to overlooking the potential influence of adherend material behavior on the failure behavior in a practical case. The fracture test is not an authentic representation of the fracture process in practice and the experimental results may not be conservative for safety design. For Fe-SMA bonded joints this has been shown in Mode II [10].

To develop a bonded and prestressed fatigue strengthening solutions using Fe-SMA, it is crucial to develop analysis tools that consider both the adherend and adhesive nonlinearities for fracture analysis of bonded Fe-SMA joints. Attempts have been made to consider the nonlinearity of bonded joint fracture behavior. The J-integral method accounts for all material nonlinearities in the fracture test [14]. More accurate values for the energy release rate were obtained for beam-like specimens [15,16]. However, this method has not been applied to study the effect of the nonlinearity of adherend materials on the fracture process. A more direct consideration of plastic deformation in the adherends during peel tests can also be found in open literature [17,18], but it is limited to thin strips with bilinear stress–strain material behavior. This work was not extended to fracture tests involving general material nonlinearities of both adherends and adhesives.

To elucidate the effect of the adherend nonlinear material behavior on the Mode I fracture behavior, DCB tests of Fe-SMA bonded joints as well as steel bonded joints carefully designed to prevent nonlinear material deformation upon testing are carried out. Based on the experimental observations and tests results, a beam on foundation model [19] considering adherend nonlinear material deformation is proposed and validated against the experimental results. The proposed model is then compared to a conventional *finite element* (FE) model to evaluate the benefits of using the proposed theoretical model. Finally a parametric study shows the effects of the Fe-SMA nonlinear material deformation on the Mode I failure process.

2. Experimental investigation

Two series of tests were executed, a series of steel to steel bonded DCB joints and another series of Fe-SMA to Fe-SMA DCB joints. The same adhesive and adhesive thickness was used. The steel to steel bonded joints used 3 mm thick high-strength steel such that the adherends remained in the elastic range throughout the experiment as the thickness was enough to avoid plastic deformation. This allowed for the experimental measurement of the *traction separation relationship* (TSR) according to established methods [16,20,21]. The samples are referred to as TS for thick steel. The second series of experiment involved thinner, Fe-SMA joints. Due to the thinness and nonlinear material behavior of the adherends, the fracture behavior was influenced by the material nonlinearity.

Table 1
Material properties and sample dimension.

Sample type	E modulus [MPa]	Yield strength σ_Y [MPa]	Thickness h [mm]	Precrack a [mm]	Adhesive
TS	181'946	923.2	3	50	SikaPower 1277
Fe-SMA	176'827	530.4	1.5	25	SikaPower 1277

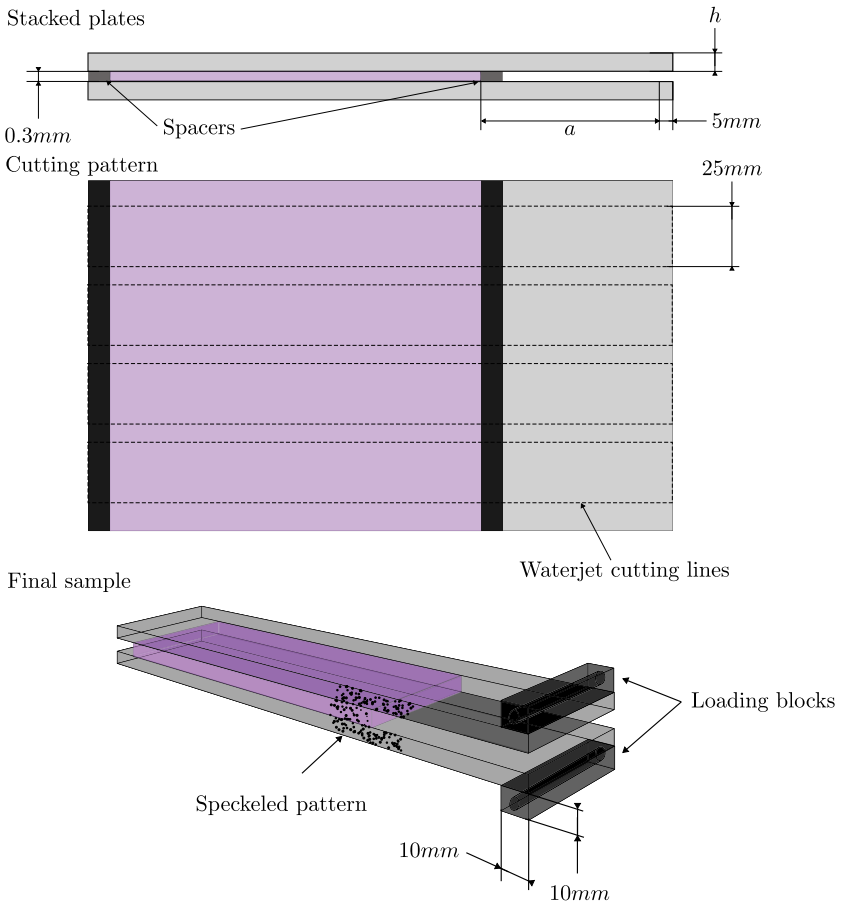

Fig. 2. Schematic of the sample preparation.

2.1. Materials and method

2.1.1. Materials

Fe-SMA was provided by re-fer AG with nominally $h = 1.5$ mm thick plates while the high-strength steel was provided by Notz Metall AG with $t = 3$ mm thick AISI 301 plates. The thickness of the Fe-SMA was constrained by the maximal plate thickness the provider could supply. It is noted that the tested Fe-SMA thickness is identical to its thickness in real application cases. Both materials were tested in tensile tests, the measured material properties are summarized in Table 1. While both materials are steels, the significant amount of alloying elements reduced the Young's modulus from usually expected values. The adhesive used was SikaPower 1277 [22].

2.1.2. Sample preparation

The sample geometry was based on ASTM D5528 [23]. The TS samples had a long precrack a and the Fe-SMA samples had shorter precrack a. This prevented geometrical nonlinear effects and isolated the influence of the material nonlinearity. Using simple beam theory, the length was chosen such that the two sample types would have a similar initial bending stiffness. The samples were prepared by bonding wider plates together then cutting by waterjet to sample size, as shown in Fig. 2. This manufacturing method was selected to limit as much as possible the heating of the Fe-SMA which can induce partial reverse phase transformation. Prior to bonding, each plate was gritblased and cleaned with acetone soaked cotton wipes. A precrack was created by inserting a 0.3 mm thick steel insert coated with release agent (Loctite 770-NC) between the plates upon bonding. A second insert was placed away from

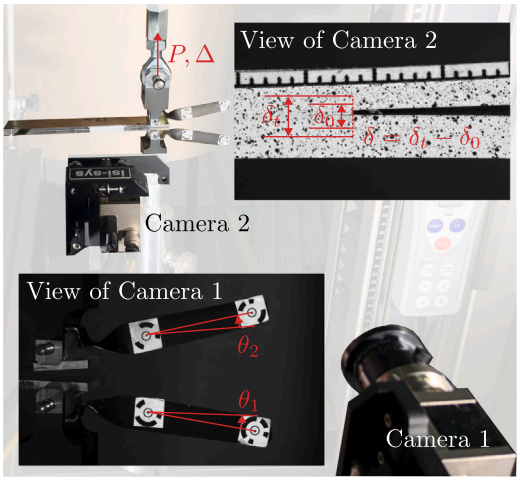

Fig. 3. Experimental setup.

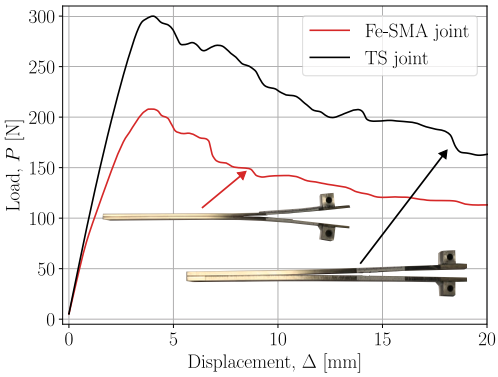

Fig. 4. Typical Load–displacement curve and tested sample deformation after test for TS and Fe-SMA joints.

the precrack to ensure a controlled adhesive thickness, as shown in Fig. 2. The plates were placed in a vacuum bag for 24 h to apply a constant and distributed pressure on the bonded plates and ensured the final adhesive thickness (vaccum pressure was 0.8 bar). The bonded specimens were then cured at room temperature for two weeks prior to cutting the samples by waterjet. The inserts were removed at this stage. The sides of every sample were polished with sandpaper to remove irregularities caused by waterjet cutting. A section of the side centered around the precrack was painted with a black speckeled pattern on white background for the DIC measurement as shown in Figs. 2 and 3. Finally loading blocks were bonded to the sample.

2.1.3. Test method

The tests were carried out on a Zwick–Roell testing machine with a 2 kN loadcell and a displacement controlled rate of 0.1 mm/s. As the tests aim at measuring the TSR, no precracking is done in order to measure the entire development of the damage region governed by cohesive behavior [16,24–26]. Two cameras were used, one was placed close to the crack tip to measure the *crack tip opening displacement* (CTOD) and the second captured a wider frame to track targets bonded to the loading blocks as shown in Fig. 3. The cameras acquisition rate was 1 Hz. The pictures were processed with Vic-2D 7.

During the test, the load, P, machine displacement, Δ, CTOD, δ, and loading blocks rotations, θ_1 and θ_2, were measured. Typical load–displacement curves for both sample types are shown in Fig. 4 along with the sample after testing. Permanent deformation is visible for both sample types. The plasticity remained limited in the TS samples as the permanent opening angle was one order of magnitude smaller than that of the Fe-SMA samples. Even in the presence of limited plasticity, the data reduction method used in the following section remains valid [20]. In the following, TS samples will be modeled as linear elastic as the loading branch of the load–displacement shows no sign of adherend yielding.

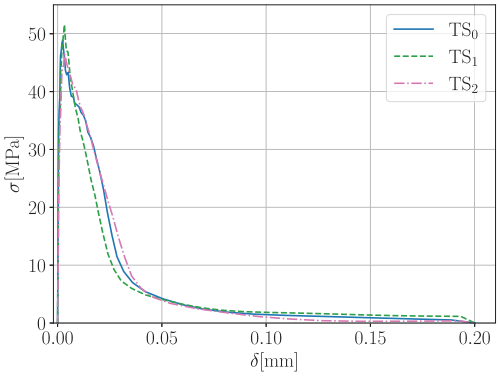

Fig. 5. Experimentally obtained TSRs with the TS samples.

2.1.4. Data reduction

To compute the fracture energy, the J-integral was used. This method was first proposed in [14] and applied for various cases [20,27–29]. In the DCB case:

$$J = \frac{P}{b}\theta \tag{1}$$

where b is the specimen width and $\theta = \theta_2 - \theta_1$ the relative rotation of the arms at the loading points, as depicted in the view of Camera 1 in Fig. 3. Note that this formulation is strictly correct only if no plastic unloading occurs [16], its application in processing the TS joints is valid but questionable for the Fe-SMA joints. Therefore, the following was carried out only for the TS samples. The TSR can be obtained from:

$$\sigma = \frac{dJ}{d\delta} \tag{2}$$

Further details on the derivation can be found in [16].

As all three quantities, P, θ, and δ were measured continuously during the test, Eq. (1) was applied directly and Eq. (2) was applied after a filtering step using a Gaussian window of J vs. time and δ vs. time and fitting a cubic spline through both signal. This prevented noise artifacts from appearing as Eq. (2) essentially consists of two time differentiation and a division. Only values for 5×10^{-4} mm $\leq \delta \leq 0.2$ mm were kept.

2.2. Experimental TSR

Three experimental TSRs obtained from the TS samples are shown in Fig. 5 and show an stiff initial slope reaching to a maximal stress of 50 MPa followed by a sharp decrease until $\delta \approx 0.05$ mm and a tail reaching 0 MPa.

3. Formulation

To model an adhesively bonded Fe-SMA DCB joint considering nonlinear material deformation as depicted in the upper schematic in Fig. 6, the beam on foundation model is used. The adherend Fe-SMA material can deform nonlinearly (see Fig. 4) and the adhesive reaction depends nonlinearly on the opening separation (see Fig. 5). The two nonlinearities are coupled by considering the adhesive action as a distributed loads on the beam, as shown in the lower schematic in Fig. 6.

3.1. Bending of a nonlinear elastic beam

A nonlinear material deformation beam model is developed first. The experimentally measured stress–strain relation of the Fe-SMA is used for the nonlinear material behavior of the beam. Classic Euler–Bernoulli beams are used to consider plastic deformation and their effects on beam behavior. The main assumption in the Euler–Bernoulli theory is that the cross-sections remain planar and normal to the beam axis after deformation [30]. Considering a short section of the beam as illustrated in Fig. 7, the relation between the horizontal displacement, u_1, and the vertical displacement, u_2, can be expressed as follows:

$$u_1 = x_2 \frac{du_2}{dx_1} \Rightarrow \epsilon_{11} = x_2 \frac{d^2u_2}{dx_1^2} \tag{3}$$

where ϵ_{11} represents strain of a material point on the beam. x_1 and x_2 represent the Cartesian coordinate system as shown in Fig. 7. For simplicity, the notation $\frac{d^n f}{dx_1^n}$ is replaced with $f^{(n)}$. The strain is assumed to be linearly distributed with respect to x_2 [30].

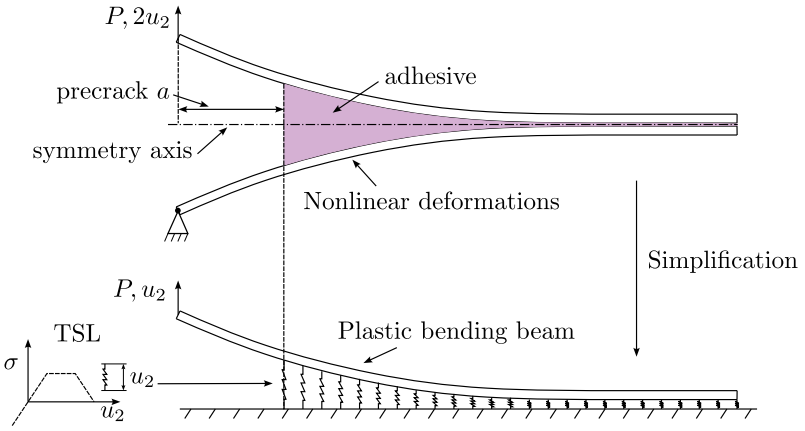

Fig. 6. Simplification of an adhesively bonded DCB to a beam on foundation model.

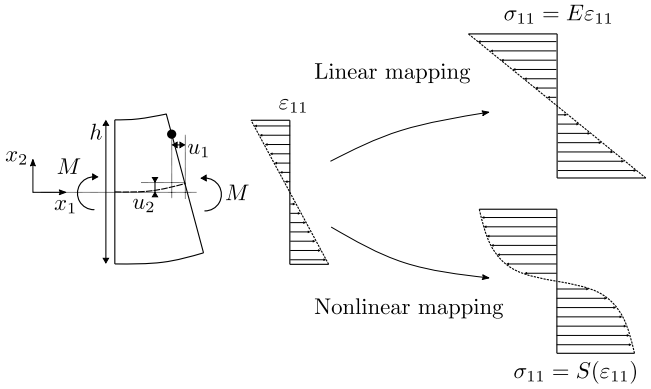

Fig. 7. Linear and nonlinear mapping between strain and stress profile.

To compute the bending moment per unit depth applied on the cross-section of height h, the stress contribution can be integrated over the beam height. When linear elasticity is assumed, as shown in the linear mapping in Fig. 7, the moment is:

$$M = \int_{-h/2}^{h/2} x_2 \sigma_{11} dx_2 = \int_{-h/2}^{h/2} x_2 E \varepsilon_{11} dx_2 = \int_{-h/2}^{h/2} x_2^2 E u_2^{(2)} dx_2 = EI u_2^{(2)} \tag{4}$$

where E is the Young's modulus and $I = \frac{h^3}{12}$ is the 2nd order moment of inertia. This results in a well-known differential equation describing a linear elastic bending beam neglecting shear loads.

When nonlinear material deformation is considered, the relationship between ε_{11} and σ_{11} is defined by a nonlinear function $\sigma_{11} = S(\varepsilon_{11})$ [30,31]. This leads to a nonlinear mapping of the stress, as shown in Fig. 7. Using the strain defined in Eq. (3), the resulting moment acting on a cross section of height h is:

$$M = \int_{-h/2}^{h/2} x_2 S(\varepsilon_{11}) dx_2 = \int_{-h/2}^{h/2} x_2 S(x_2 u_2^{(2)}) dx_2 \tag{5}$$

where M has therefore only $u_2^{(2)}$ as a variable. The relationship between the local bending moment per unit depth and local curvature $u_2^{(2)}$ is entirely defined by h and $\sigma_{11} = S(\varepsilon_{11})$. This is expressed as follows:

$$M = F(u_2^{(2)}) \tag{6}$$

In the present case, $S(\varepsilon_{11})$ is measured experimentally rather than described by an analytic expression. The nonlinear stress–strain relationship of Fe-SMA measured in a tensile test is employed to represent $S(\varepsilon_{11})$, as shown in Fig. 8(a). The tension and compression behavior are assumed to be the same as shown in Fig. 8(a).

In a strain controlled loading–unloading of the material, the function $S(\varepsilon_{11})$ will give the same stress response in both loading and unloading stages. The physical Fe-SMA will retain part of its deformation if unloaded and thus should be described with an elasto-plastic material behavior. However, in a pure loading stage, elasto-plasticity and nonlinear elasticity are indistinguishable and the treatment of the material behavior as a function facilitates further developments of the model. In a DCB test, the loading is

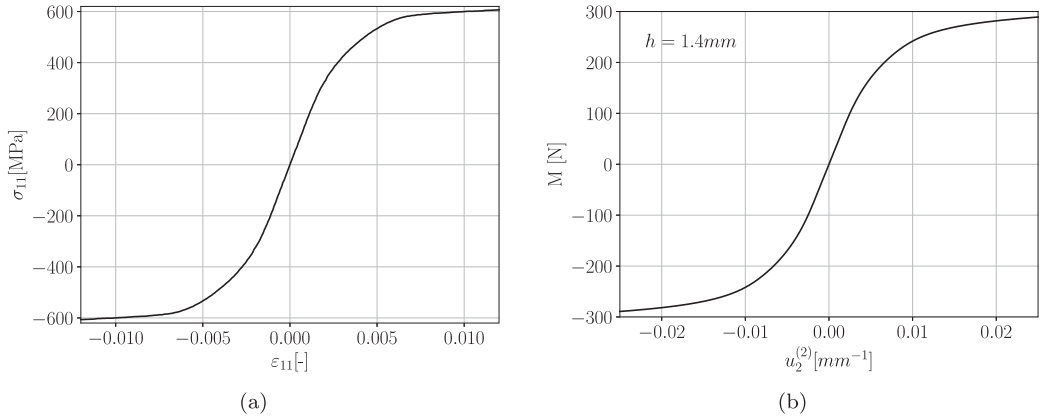

Fig. 8. (a) $\sigma_{11} = S(\varepsilon_{11})$ represented by experimental Fe-SMA tensile test data. (b) The associated $M = F(u_2^{(2)})$ function.

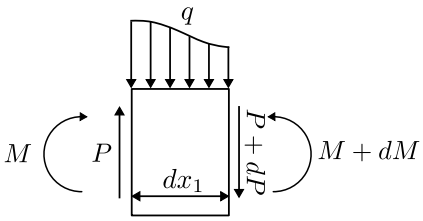

Fig. 9. Infinitesimal beam cross-section.

not monotonic and the adherend is subjected to unloading as the critical load reduces with crack propagation, as shown in Fig. 4. It is assumed that up to crack initiation, the unloading in the adherends is limited, therefore limiting the influence of the simplified material behavior treatment.

Linear interpolation and trapezoidal integration is used to compute $M = F(u_2^{(2)})$ from the experimental $\sigma_{11} - \varepsilon_{11}$ data. The integrand $x_2 S(x_2 u_2^{(2)})$ is obtained for every $-h/2 \leq x_2 \leq h/2$ by linear interpolation in the experimental data representing $S(\varepsilon_{11})$ for a range $u_2^{(2)}$ by discretization of the integration domain $[-h/2, h/2]$. Finally, the trapezoidal integration of the integrand over the domain $[-h/2, h/2]$ allows the evaluation of bending moment per unit depth associated with $u_2^{(2)}$. An example of the resulting function is presented in Fig. 8(b) for $h = 1.4$ mm.

As $\sigma_{11} = S(\varepsilon_{11})$ is assumed to be strictly monotonic and increasing, $M = F(u_2^{(2)})$ is as well, it implies that $u_2^{(2)} = F^{-1}(M)$ exists. If the bending moment in the beam is known, so is its local curvature. This is the case for the unbonded region of the DCB specimen. Given a precrack length a and an applied load P, the bending moment per unit depth is $M = P(a - x_1)$, neglecting nonlinear geometrical effects. Because $M(x_1)$ is known the curvature $u_2^{(2)}(x_1) = F^{-1}(P(a - x_1))$ can be calculated.

Integrating this twice from 0 to a,

$$u_2(a) = \int_0^a \int_0^\xi u_2^{(2)}(\eta) d\eta d\xi + a u_2^{(1)}(0) + u_2(0) \tag{7}$$

where $u_2^{(1)}(0)$ and $u_2(0)$ are the boundary conditions representing the root rotation and δ, respectively.

3.2. Nonlinear elastic beam on foundation

In the bonded region, the adhesive layer is continuously bonded to the beam. To couple the adhesive and the layer, an externally distributed load on the nonlinear beam is considered and this distributed load is then associated to the layer reaction force. First, the infinitesimal element depicted in Fig. 9 is considered.

Static equilibrium must be maintained; thus, the following conditions must to be met:

$$\frac{dM}{dx_1} = P \tag{8}$$

$$\frac{dP}{dx_1} = -q \Rightarrow \frac{d^2M}{dx_1^2} = -q \tag{9}$$

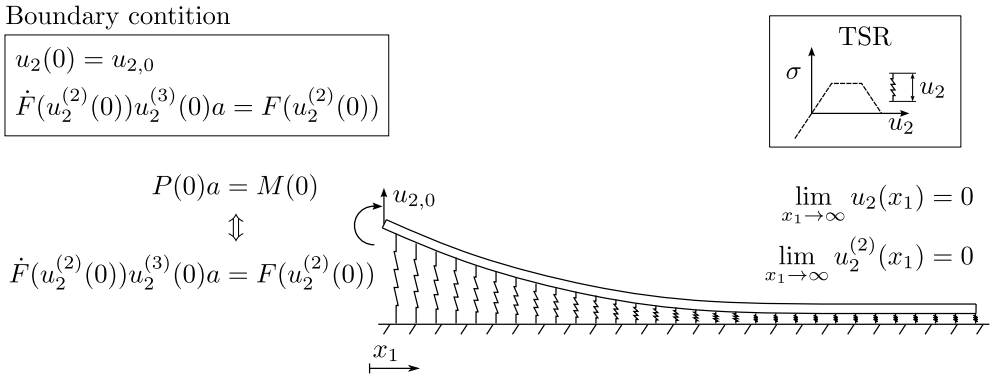

Fig. 10. Schematic of studied problem with prescribed boundary conditions.

Recalling Eq. (6):

$$\frac{dM}{dx_1} = \frac{dF(u_2^{(2)})}{dx_1} = \frac{dF(u_2^{(2)})}{du_2^{(2)}}u_2^{(3)} = P \tag{10}$$

$$\frac{d^2M}{dx_1^2} = \frac{d^2F(u_2^{(2)})}{d(u_2^{(2)})^2}(u_2^{(3)})^2 + \frac{dF(u_2^{(2)})}{u_2^{(2)}}u_2^{(4)} = -q \tag{11}$$

For simplicity, the notation $\dot{F} = \frac{dF}{du_2^{(2)}}$ is used hereafter. Until here no assumptions have been made regarding the distributed load q. If the modeled problem is meant to represent the debonding of an adhesive layer, the normal stress should first increase with the opening u_2, reach a maximum, and then decrease until the adhesive is completely damaged as in Fig. 5. This relationship is denoted as $\sigma(u_2)$. Therefore,

$$M^{(2)} = \ddot{F}(u_2^{(2)})(u_2^{(3)})^2 + \dot{F}(u_2^{(2)})u_2^{(4)} = -\sigma(u_2) \tag{12}$$

Eq. (12) is the general equation describing the deflection of a nonlinear beam on a foundation described by a TSR with any shape. Two nonlinearities, the beam material nonlinearity via $\ddot{F}(u_2^{(2)})(u_2^{(3)})^2$ and the adhesive nonlinearity via $\sigma(u_2)$ are combined. If linear elasticity in the beam and the foundation is assumed, then $F(u_2^{(2)}) = EIu_2^{(2)}$ and $\sigma(u_2) = ku_2$, and Eq. (12) reduces to

$$EIu_2^{(4)} + ku_2 = 0 \tag{13}$$

which is a form found in [19]. Eq. (12) is a generalization of the augmented cantilever beam that takes two nonlinear behaviors into account.

3.3. Boundary conditions

External load on the beam is applied through the means of boundary conditions. It is preferable to express the boundary conditions in terms of displacement to represent a stable, displacement-controlled fracture test. These boundary conditions are essential for solving the developed differential equation.

The representative loading case illustrated in Fig. 10 is investigated. The beam is fully bonded from $x_1 = 0$ to the end. A displacement and the corresponding reacting moment $M = Pa$ are applied at $x_1 = 0$. This loading scenario represents a DCB test with a precrack length of a.

The beam is not loaded from the crack tip but rather from a precrack length a and a non-zero bending moment is applied at the crack tip at $x_1 = 0$. The transversely reacting load at the crack tip is given by

$$P = M^{(1)} = \dot{F}(u_2^{(2)})u_2^{(3)} \tag{14}$$

In the unbonded region of the beam, the transverse load P is constant; thus, the bending moment M applied at the crack tip is Pa if small displacements are assumed. The following continuity condition must fulfilled.

$$P(0)a = M(0) \iff \dot{F}(u_2^{(2)}(0))u_2^{(3)}(0)a = F(u_2^{(2)}(0)) \tag{15}$$

Eq. (15) gives a boundary condition if the problem modeled is a beam loaded from a distance a. Finally, to obtain the end-beam deflection, Eq. (7) is used with the root rotation $u_2^{(1)}(0)$ given by the solution of Eq. (12) and the applied displacement $u_2(0) = u_{2,0}$.

The TSR in Fig. 10 represents a possible behavior of the reaction force opposed by the springs, and the behavior is defined in both tension and compression.

3.4. Numerical solutions

The differential Eq. (12) is solved numerically for two reasons. First, $F(u_2^{(2)})$ is calculated numerically, as detailed in Section 3.1, and there is no analytical expression available. Second, no constraints are imposed on the TSR, $\sigma(u_2)$, which preserves the generality of the model. A reformulation of the problem and boundary conditions such that it can be solved as a vector *boundary value problem* (BVP) is presented.

With the following substitutions, the problem can be expressed as a first-order *ordinary differential equation* (ODE) with a vector variable:

$$\begin{aligned} f_4^{(1)} &= u_2^{(4)} = -\frac{\ddot{F}(f_3)}{\dot{F}(f_3)} f_4^2 - \frac{\sigma(u_2)}{\dot{F}(f_3)} \\ f_3^{(1)} &= u_2^{(3)} = f_4 \\ f_2^{(1)} &= u_2^{(2)} = f_3 \\ u_2^{(1)} &= f_2 \end{aligned} \tag{16}$$

Eq. (12) in vector form is given by Eq. (17).

$$\frac{d\boldsymbol{y}}{dx_1} = \boldsymbol{f}(x_1, \boldsymbol{y}) \text{ with } \boldsymbol{y} = \begin{bmatrix} f_4 \\ f_3 \\ f_2 \\ u_2 \end{bmatrix}, \boldsymbol{f}(x_1, \boldsymbol{y}) = \begin{bmatrix} -\frac{\ddot{F}(f_3)}{\dot{F}(f_3)} f_4^2 - \frac{\sigma(u_2)}{\dot{F}(f_3)} \\ f_4 \\ f_3 \\ f_2 \end{bmatrix} \tag{17}$$

Accordingly, the boundary conditions are described by Eq. (18).

$$\begin{cases} \lim_{x_1 \to \infty} f_3(x_1) & = 0 \\ \lim_{x_1 \to \infty} u_2(x_1) & = 0 \\ \dot{F}(f_3(0)) f_4 a & = F(f_3(0)) \\ u_2(0) & = u_{2,0} \end{cases} \tag{18}$$

As the numerical domain cannot be infinite, the solution is solved for a finite length domain, which is assumed to be longer than the *fracture process zone* (FPZ). Eqs. (6), (17) and (18) are implemented in Python, and the SciPy library [32] used to numerically solve the BVP. The internal algorithm is based on a 4th order collocation algorithm with residual control [33].

A flowchart of the implementation is presented in Fig. 11. First, $F(u_2^{(2)})$ is computed using trapezoidal integration, and a cubic spline is fitted through the resulting relationship. This allows for smooth evaluation of F, $\dot{F}$, and $\ddot{F}$. Two functions are required to solve the system: one that returns $\boldsymbol{f}(\boldsymbol{y})$ and one that returns four residuals (one per boundary condition). The system is solved using the SciPy routine `solve_bvp`.

3.5. Experimental validation

The tests carried out in Section 2 are used to validate the proposed model. The tested samples are modeled and the TSRs used are the ones presented in Fig. 5 where the CTOD has been halved. As the model is a beam laying on a rigid ground representing the symmetry axis of the DCB sample, as illustrated in Fig. 6, the displacement at the crack tip in the model is half of the experimental CTOD and the displacement at the loaded end is half of the experimental displacement.

Using a TSR measured with TS joints to model Fe-SMA joints assumes that the fracture energy and the TSR shape are material properties of the adhesive and independent on the adherends. While this is accepted for the fracture energy [34,35], contradicting results can be found regarding the shape of the TSR [36,37].

Solutions are computed for a range of CTODs. To compute the reaction load per unit depth on the beam from the solution, Eq. (19) derived from Eq. (14) is used.

$$P_{react} = \dot{F}(u_2^{(2)}(0)) u_3^{(3)}(0) = \dot{F}(f_3(0)) f_4(0) \tag{19}$$

The resulting modeled load-CTOD and load–displacement curves are shown in Fig. 12, along with experimental ones. The experimental load is normalized per unit width and the experimental CTOD and displacement halved.

Good agreement is found for the TS joints both in the load–displacement and load-CTOD curves (Figs. 12(b) and 12(a)). In the Fe-SMA joints case, good agreement in the load-CTOD comparison, especially the fracture initiation ($0 \text{ mm} \leq \text{CTOD} \leq 0.1 \text{ mm}$) is found in Fig. 12(c). As for load–displacement case, Fig. 12(d) shows the initial stiffness appears to be overestimated. Nonetheless, the bond strength can be well approximated.

The proposed method can predict the bond strength of adhesively bonded joints given the TSR corresponding to the adhesive used. If linear elastic adherends are used the model is able to predict the CTOD and the loading point displacement during the fracture initiation process. If nonlinear adherends are used and assuming TSRs are adhesive material properties, the model can predict the CTOD. For the displacement of the loading point, the model prediction deviate from the experiments. The lever length a will magnify small root rotation errors and induce a large error in the end-beam displacement, see Eq. (7). The other explanation may be that TSR shapes are dependent on the adherends and that the TSR should be adjusted if used to model Fe-SMA joints. This should be done in a way that preserves the fracture energy. However, this question is left outside the scope of the present work and for future investigations.

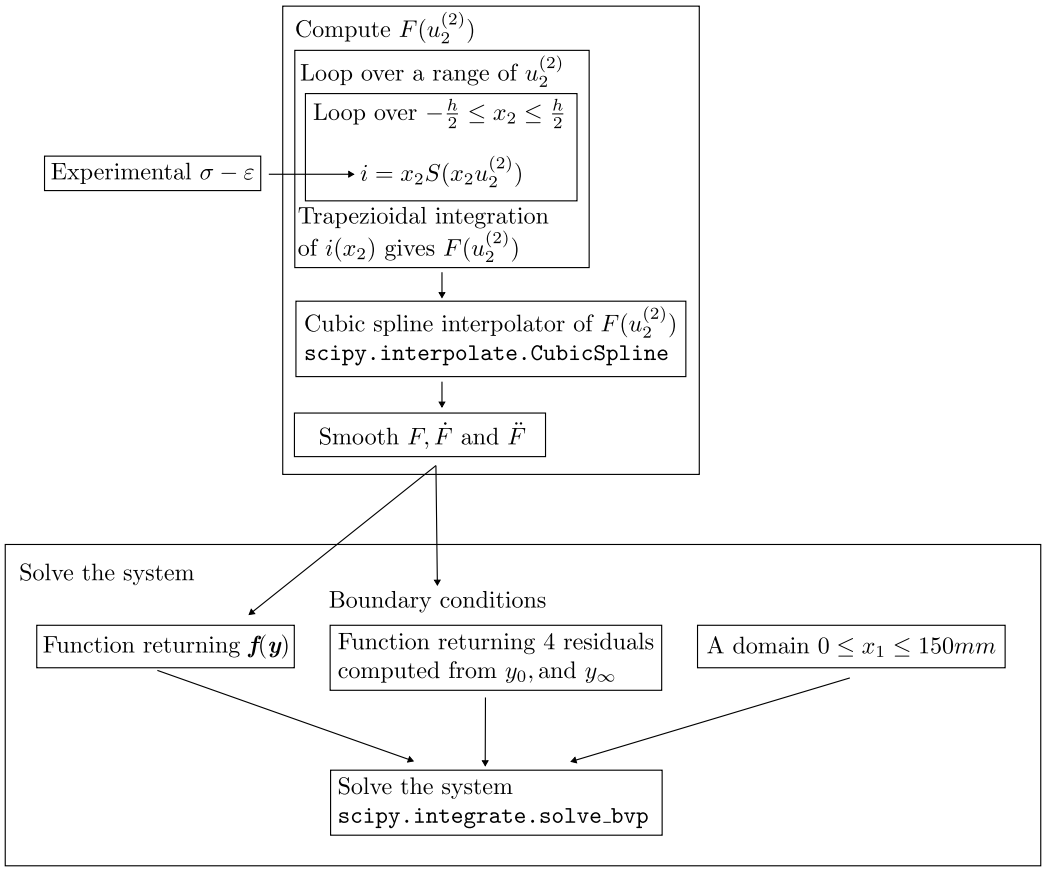

Fig. 11. Implementation flowchart for solving the differential Eq. (12).

4. Comparison to finite elements method

The proposed theoretical model offers a non-incremental method to model fracture of bonded joints which relies on the analytical formulation of the problem at hand and a generic boundary value problem solver. This offers a fast and straightforward way to gain insight in a bonded joint behavior. Other methods with the same capabilities exist, with the most popular being a *finite element* (FE) model considering elasto-plastic material behavior and *cohesive zone modeling* (CZM) interaction. To further evaluate the proposed theoretical model's accuracy and performance it is compared to such an FE model.

A model representing the problem in Fig. 10 is built using ABAQUS [38]. It consists of a 2D beam and a rigid body 1D ground. The beam is assigned an elasto-plastic material model with the yield stress-plastic strain relationship depicted in Fig. 13.

A simpler trapezoidal TSR shown in Fig. 14(a) was used for the sake of comparison. The cohesive interface is defined by setting a cohesive contact between the rigid ground and the beam, and the damage evolution is defined with tabulated data giving the evolution of the damage (D) with the plastic displacement (U). Both are defined in Eqs. (20) and (21). No interaction is defined for a length corresponding to the initial crack length a.

$$D = 1 - \frac{\sigma(u_2)/u_2}{K} = 1 - \frac{K_D}{K} \tag{20}$$

$$U = u_2 - u_{2,init} \tag{21}$$

Here, K is the undamaged stiffness and K_D is the damaged stiffness of the cohesive interaction, as depicted in Fig. 14.

No additional penalty stiffness is required as cohesive interaction is also defined for a negative opening in ABAQUS allowing to model the compression of the adhesive layer. The penetration is expected to be smaller than the damage initiation displacement, so it perfectly mimics an elastic compressive branch, as shown in the insert in Fig. 10.

The rigid ground is completely constrained, and no displacement is allowed. At the free end of the beam, the vertical displacement is set to zero (second condition in Eq. (18)). A vertical displacement is defined at the loaded end.

The model and boundary conditions are summarized in Fig. 15. The FE model is discretized using plane stress linear quadrilateral elements. The elements aspect ratio is one and the element edge length is 0.175 mm.

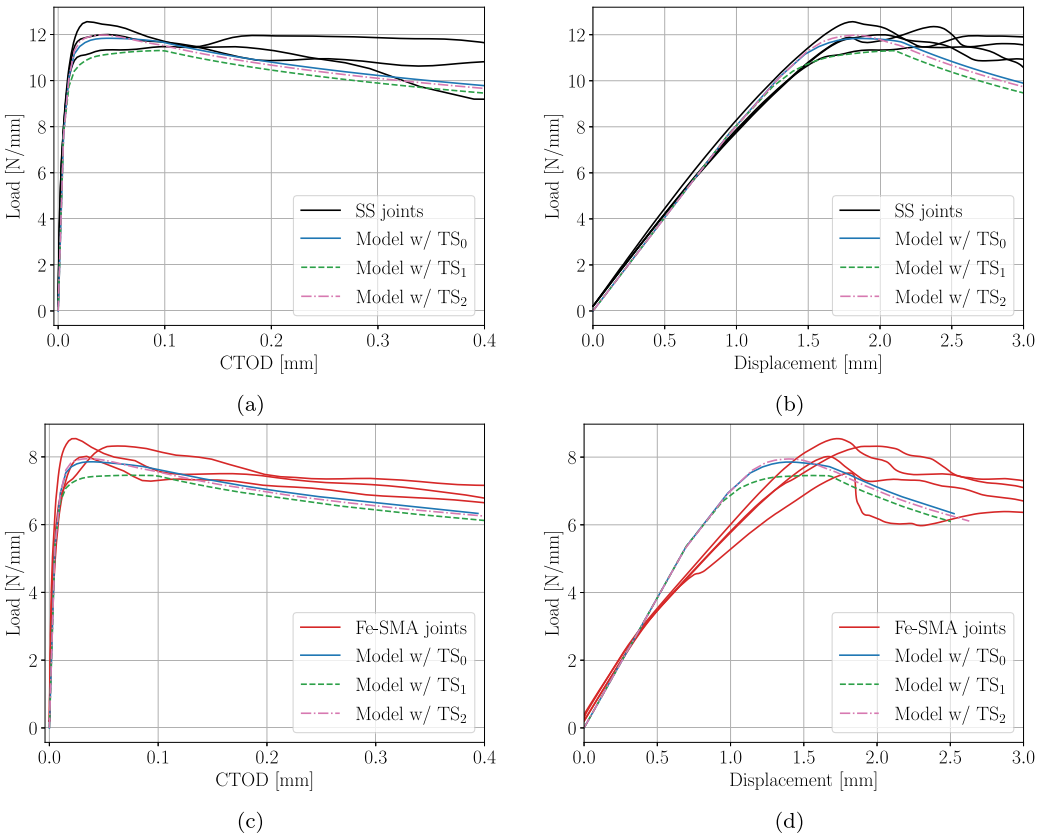

Fig. 12. Validation against experimental DCB test results. (a) Load-CTOD curves for TS samples. (b) Load–displacement curves for TS samples. (c) Load-CTOD curves for Fe-SMA samples. (d) Load–displacement curves for Fe-SMA samples.

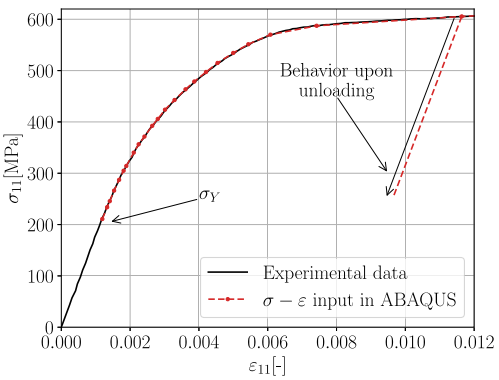

Fig. 13. The stress–strain relationship of Fe-SMA defined in FE modeling.

4.1. DCB model comparison

A 150 mm long beam of 1.4 mm thickness laying on a foundation depicted in Fig. 15 is modeled with both methods. The TSR used is shown in Fig. 14(a). The material behavior defined is based on the experimental $\sigma_{11} - \varepsilon_{11}$ tensile test of Fe-SMA results (Figs. 8(a) and 13). The precrack length is chosen as $a = 25$ mm. Fig. 16 presents the results under an imposed displacement of $u_{2,0} = 0.2, 0.5, 1.0$ mm. Fig. 16(a) presents solutions for the beam deflection and the corresponding reaction forces opposed by the adhesive layer. In Fig. 16(b), the load-CTOD curves provided by both models are shown. In Fig. 16(c), the load–displacement curves are shown.

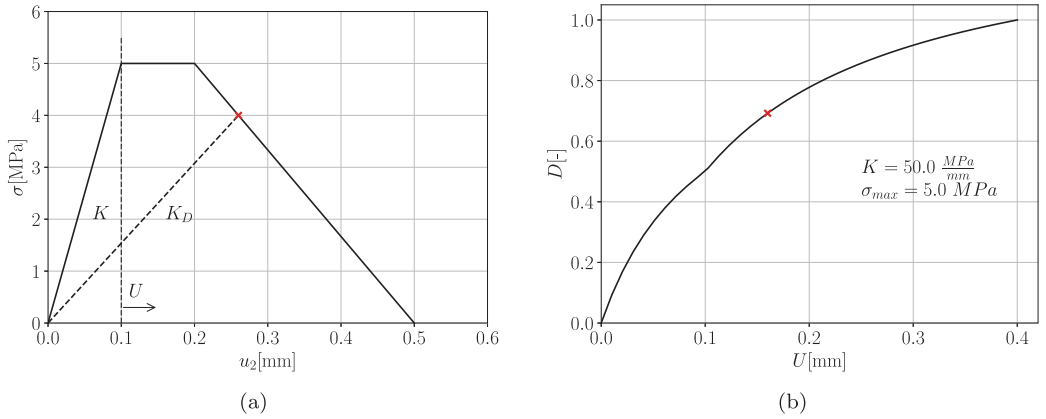

Fig. 14. Transformation of the TSR to damage evolution data as used in FE. (a) As used in model, represented as $\sigma(u_2)$. (b) The corresponding damage evolution relationship, as represented in FE.

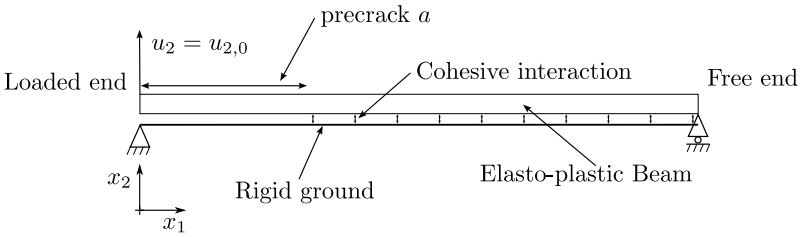

Fig. 15. Finite element model with the boundary conditions.

All three solutions depicted in Fig. 16(a) are consistent with the FE model. Furthermore, Fig. 16(b), which shows the applied load over the CTOD, confirms that the model is consistent with the FE model throughout the debonding process. The main assumption of Section 3.1 appears valid.

Both curves drift apart after the ultimate load is reached, a similar effect is seen in Fig. 12. This is because of the fundamental difference between the material definition of both models. Upon unloading, the elasto-plastic material retains part of its deformation as in Fig. 13. Therefore, the FE predicted load–displacement exhibits a higher displacement for the same load after the maximum load is reached (start of unloading). This explains the difference between the two models, which is amplified by the initial lever arm length, a.

What sets the models apart is their computational cost. While FE offers a versatile and robust method to analyze general structural problems, the simplified model dedicated to a single problem will be computationally less expensive. While it may be hard to compare two algorithms' performance objectively, some reasonable comparisons can be made.

To produce the results in Fig. 16, the proposed theoretical model computes 70 solutions with the boundary conditions spanning $0\ \text{mm} \leq u_{2,0} \leq 1\ \text{mm}$, this required on average 8.53 ± 0.58 s (the process was repeated 50 times to get an average value). The FE model computed 63 steps in 58.93 ± 3.00 s using 4 cpus (the process was repeated 10 times to get an average value). Both computations were performed on the same computer, in the same conditions, with no other resource-consuming process running.

While the effective computing time can be influenced by many factors and these results regarded with the necessary caution, this suggests a better performance of the proposed theoretical model. It is about seven times faster than the FE. If the user requires only a single solution and not the full load–displacement behavior, the fact that the proposed theoretical model is non-incremental further puts it at an advantage.

5. Comparison with linear elastic beams

The significance of this new model lies in its consideration of adherend material nonlinearity. The influence of this beam on foundation model extension is estimated by comparing it to that of a linear elastic adherends. Two parallel models are compared in this section. One with an experimental stress–strain curve describing a nonlinear relationship, the same model as in Section 3.5 and a second identical model only with a Young's modulus $E = 176'827$ MPa (as in Table 1). The TSR used is TS_2 in Fig. 5.

The output of both models are presented in Fig. 17. The difference between the beams' behaviors is limited, as the nonlinear beam remains close to the linear region (see Fig. 17(c)) due to limited precrack and adhesive toughness.

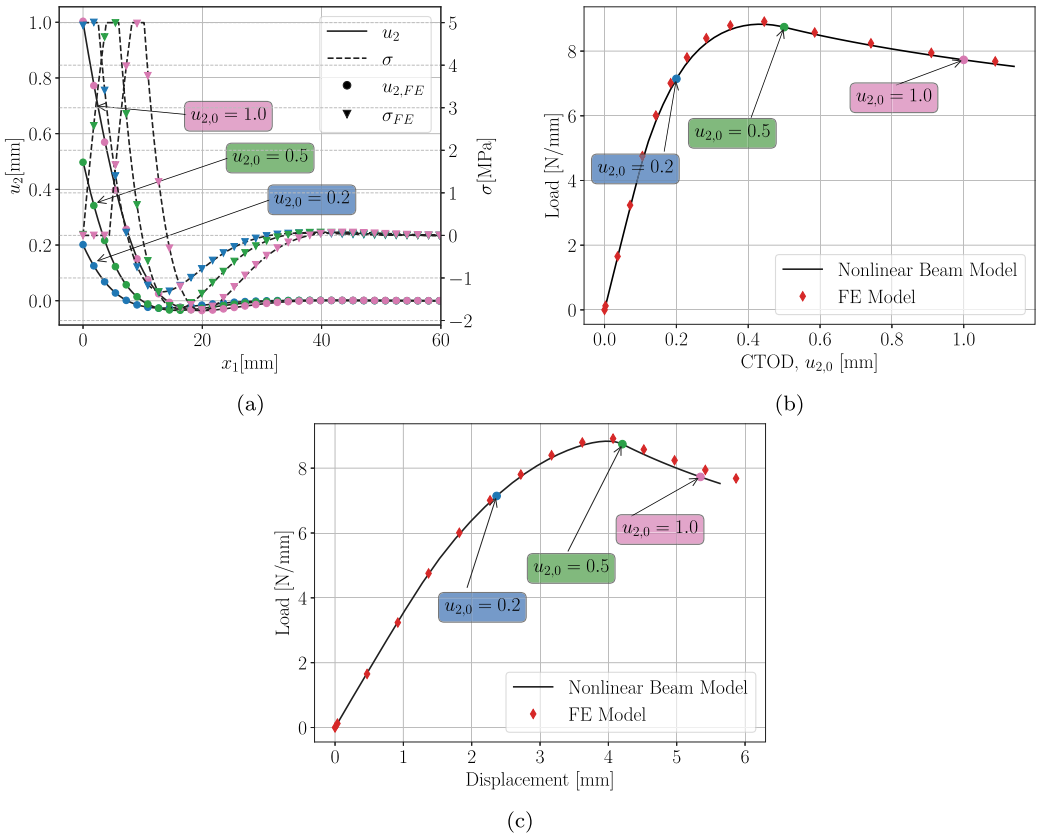

Fig. 16. Validation against FE for a partially bonded beam. (a) The deflection of the beam and reaction forces opposed by the adhesive layer at different imposed boundary conditions. (b) The predicted load-CTOD curves. (c) The predicted load–displacement curves.

Fig. 18 shows the effect of beam nonlinear material deformation on the output of the model used in Section 4.1 using a tougher adhesive. The TSR used is shown in Fig. 14(a). Fig. 18(b) shows the ultimate load is lower by 9.5% in the presence of nonlinear material deformation. The differences are more obvious as the bending moment increases beyond the local linear range in Fig. 18(c).

These differences are explained because the fracture process is inherently a displacement controlled failure process. Adhesive fracture occurs at a critical displacement where the traction reaches zero (in Fig. 5 $u_{2,critical} = 0.2$ mm and in Fig. 14, $u_{2,critical} = 0.5$ mm). When an infinitesimal section of the adhesive undergoes the same stress–strain history and dissipates the same amount of energy (same TSR), an infinitesimal section of the beam requires less energy to reach compatible deformation. The overall external work is lower, as shown in Fig. 18(b).

For the same reason, the FPZ, defined as the region within which damage accumulates, is shorter in the nonlinear case than the linear case (see Fig. 18(a)).

The impact of the material behavior in the bonded region is expected; as the highest bending moment, therefore highest stress, is located in the vicinity of the crack tip. However, models from the literature do not consider the possibility of local yielding of adherends [39–42].

This study does not aim to demonstrate that elastic adherends result in higher bond strengths. Instead, it points out the effect of not considering nonlinear material deformation in the adherends. Bonded lightweight metallic structures undergo plastic deformation upon joint failure. This is unavoidable because of the thinness of adherends. The results show that the assumption of linear elastic adherends leads to an overestimation of the bond strength, as nonlinear deformation causes premature joint failure. Although the presence of two dissipative mechanisms may initially be assumed to increase the bond strength, the inverse occurs as the increased deformation in the adherends increases the CTOD.

6. Advantages and limitations of the model

The proposed method is able to model the problem of the monotonic debonding of a strip with nonlinear material deformation bonded to any type of nonlinear adhesive with results in accordance with FE methods and is validated by experiments. Contrary to FE, the model is non-incremental, allowing for direct computation of the solution given a set of boundary conditions without handling nonlinearities through incremental steps. This allows for faster execution, about seven times faster.

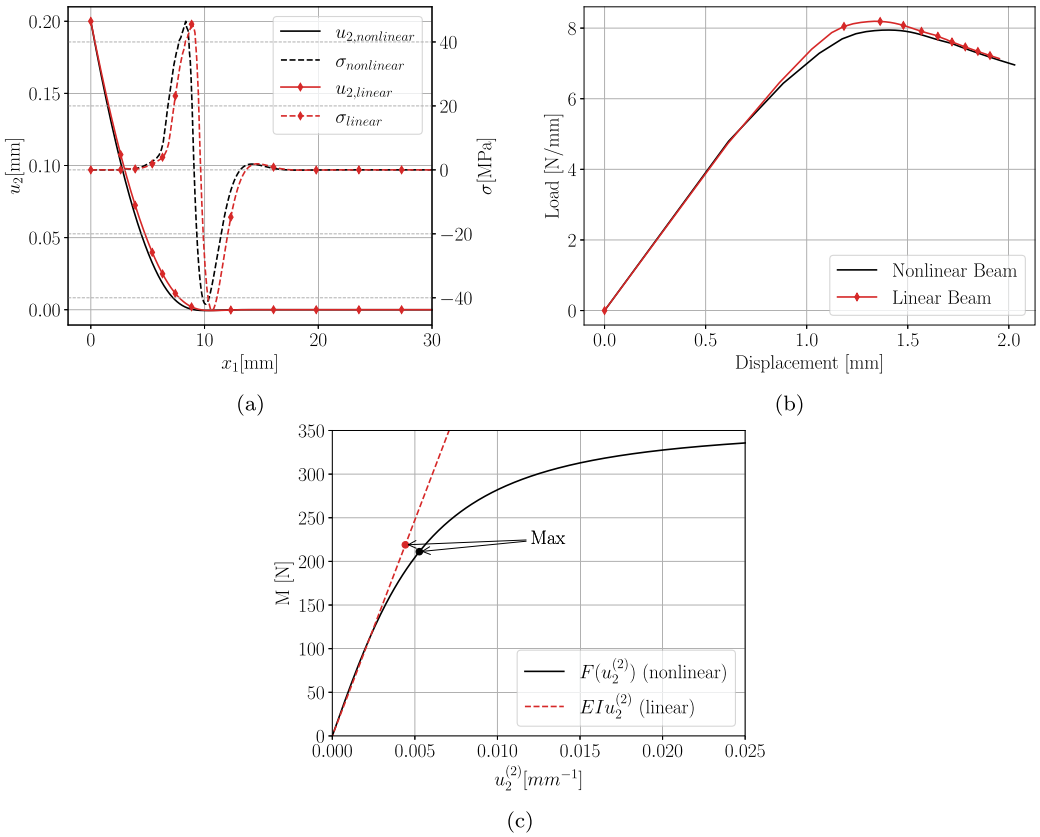

Fig. 17. Comparison between a linear and nonlinear elastic beam (a) Deflection and reaction force of the cohesive layer for $u_{2,0} = 0.2$ mm. (b) Load–displacement curves. (c) Moment–curvature relationship both beams with highest moment and curvature in the beam at initiation ($u_{2,0} = 0.1$ mm).

Recovering the TSR using the load–displacement curve and unidirectional $\sigma_{11} - \varepsilon_{11}$ diagram, appears feasible given the rapid execution. Such an approach was proposed recently for hardwood bonded joints [43]. Using this model can allow for the reverse identification of the TSR, accounting for the nonlinear material behavior of the adherends and completely decoupling both nonlinearities; however, this is beyond the scope of this work.

Nonetheless, the present work has several limitations worth pointing out and discussing. The first is a simplified treatment of nonlinear material deformation behavior. As mentioned, this approach assumes that the adherends are nonlinear elastic, and thus history-independent. This allows for the formulation of Eq. (12), but deviates from reality when unloading occurs. However, Fig. 16 shows that the difference only manifests after the crack has completely initiated. The treatment of CZM suffers from the same drawback as an unloading actually results in a "rebonding". No history-dependent damage variables are considered. The model is only equivalent to an elasto-plastic model with damage accumulation in the adhesive during monotonic debonding. This holds for all other analytical closed-form solutions.

The second limitation is the use of a modified Euler–Bernoulli beam with inherent limitations. Only small strains and deformations are valid; therefore, the unbonded length needs to be short, as a long precrack will lead to large displacements at the loaded end, which is outside the validity range of the model. For the load–displacement curve presented in Fig. 16, the impact of the geometric nonlinear deformation is investigated via FE. The maximal error of the reaction load is below 1.3%, whereas the difference due to material nonlinearity on the reaction force is about 9.5% in Fig. 18.

7. Conclusion

Mode I fracture behavior of Fe-SMA and steel bonded DCB joints were investigated experimentally and theoretically to deepen the understanding of the influence of Fe-SMA nonlinear material behavior on the joint failure behavior. The main findings of this study are as follows:

- Fe-SMA to Fe-SMA DCB joints were tested and the Fe-SMA material exhibited nonlinear deformation when compared to steel to steel DCB test results.
- A new theoretical model has been developed and validated against experimental results. It successfully predicts the ultimate bond strength for the Fe-SMA joints.

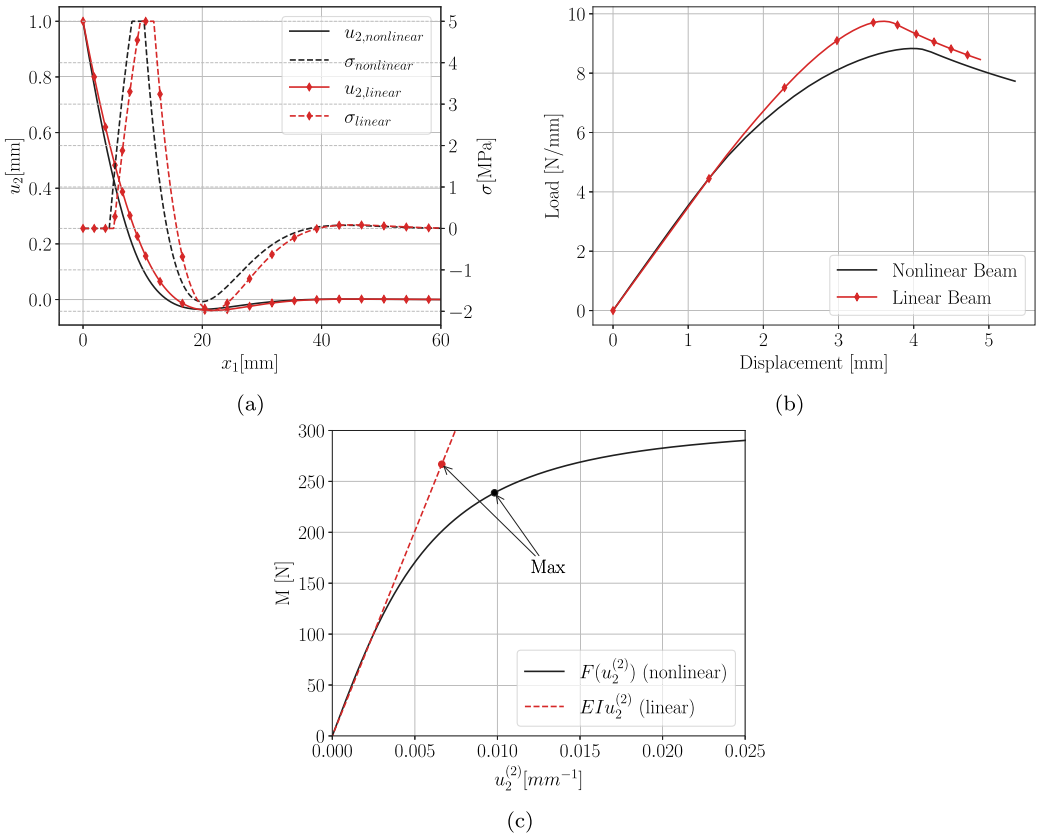

Fig. 18. Comparison between a linear and nonlinear elastic beam (a) Deflection and reaction force of the cohesive layer for $u_{2,0} = 1$ mm. (b) Load–displacement curves. (c) Moment–curvature relationship both beams with highest moment and curvature in the beam at initiation ($u_{2,0} = 0.5$ mm).

- The model captures the interaction of the nonlinear deformations of adhesive and adherend. It shows the influence of the adherend material nonlinearity on the failure mechanism is to reduce the bond strength by increasing the crack tip displacement.
- The model is based on a differential equation solved with a general boundary value problem solver openly available. While it comes with some limitations, the theoretical model is non-incremental and was found to be faster than conventional FE methods to predict the Mode I failure of Fe-SMA bonded joints while considering the nonlinear material behavior.
- The model can be further used to analyze DCB tests in the presence of unavoidable nonlinear material deformation to extract TSRs using only adherend stress strain data from a unidirectional tensile test and experimental load–displacement curves.

CRediT authorship contribution statement

Niels Pichler: Visualization, Software, Methodology, Investigation, Formal analysis, Conceptualization, Writing – original draft. **Wandong Wang:** Writing – original draft, Supervision. **Masoud Motavalli:** Writing – review & editing. **Andreas Taras:** Writing – review & editing. **Elyas Ghafoori:** Writing – review & editing, Supervision.

Declaration of competing interest

The authors declare that they have no known competing financial interests or personal relationships that could have influenced the work reported in this paper.

Data availability

Data will be made available on request.

Acknowledgments

The authors would like to acknowledge the financial support of the Swiss National Science Foundation, SNSF (Grant No. 200021_192238), and re-fer AG for providing the material used for this work.

References

[1] Wang W, Li L, Hosseini A, Ghafoori E. Novel fatigue strengthening solution for metallic structures using adhesively bonded fe-sma strips: A proof of concept study. Int J Fatigue 2021;148:106237. http://dx.doi.org/10.1016/j.ijfatigue.2021.106237.
[2] Wang S, Li L, Su Q, Jiang X, Ghafoori E. Strengthening of steel beams with adhesively bonded memory-steel strips. Thin-Walled Struct 2023;189:110901. http://dx.doi.org/10.1016/j.tws.2023.110901.
[3] Wang W. On the finite width correction factor in prediction models for fatigue crack growth in built-up bonded structures. Eng Fract Mech 2020;107156. http://dx.doi.org/10.1016/j.engfracmech.2020.107156.
[4] Li L, Wang S, Chen T, Chatzi E, Heydarinouri H, Ghafoori E. Fatigue strengthening of cracked steel plates with bonded Fe-SMA strips. ce/papers 2023;6(3–4):380–4. http://dx.doi.org/10.1002/cepa.2559.
[5] Shahverdi M, Michels J, Czaderski C, Motavalli M. Iron-based shape memory alloy strips for strengthening RC members: Material behavior and characterization. Constr Build Mater 2018;173:586–99. http://dx.doi.org/10.1016/j.conbuildmat.2018.04.057.
[6] Fritsch E, Izadi M, Ghafoori E. Development of nail-anchor strengthening system with iron-based shape memory alloy (fe-sma) strips. Constr Build Mater 2019;229:117042. http://dx.doi.org/10.1016/j.conbuildmat.2019.117042.
[7] Izadi M, Motavalli M, Ghafoori E. Iron-based shape memory alloy (fe-sma) for fatigue strengthening of cracked steel bridge connections. Constr Build Mater 2019;227:116800. http://dx.doi.org/10.1016/j.conbuildmat.2019.116800.
[8] Izadi M, Hosseini A, Michels J, Motavalli M, Ghafoori E. Thermally activated iron-based shape memory alloy for strengthening metallic girders. Thin-Walled Struct 2019;141:389–401. http://dx.doi.org/10.1016/j.tws.2019.04.036.
[9] Li L, Wang W, Chatzi E, Ghafoori E. Experimental investigation on debonding behavior of Fe-SMA-to-steel joints. Constr Build Mater 2023;364:129857. http://dx.doi.org/10.1016/j.conbuildmat.2022.129857.
[10] Li L, Chatzi E, Ghafoori E. Debonding model for nonlinear Fe-SMA strips bonded with nonlinear adhesives. Eng Fract Mech 2023;282:109201. http://dx.doi.org/10.1016/j.engfracmech.2023.109201.
[11] Wang W, De Freitas ST, Poulis JA, Zarouchas D. A review of experimental and theoretical fracture characterization of bi-material bonded joints. Composites B 2021;206:108537. http://dx.doi.org/10.1016/j.compositesb.2020.108537.
[12] Tsokanas P, Loutas T, Nijhuis P. Interfacial fracture toughness assessment of a new titanium–CFRP adhesive joint: An experimental comparative study. Metals 2020;10(5):699. http://dx.doi.org/10.3390/met10050699.
[13] Wang W, Lopes Fernandes R, Teixeira De Freitas S, Zarouchas D, Benedictus R. How pure mode I can be obtained in bi-material bonded DCB joints: A longitudinal strain-based criterion. Composites B 2018;153:137–48. http://dx.doi.org/10.1016/j.compositesb.2018.07.033.
[14] Paris AJ, Paris PC. Instantaneous evaluation of J and C. Int J Fract 1988;38(1):R19–21. http://dx.doi.org/10.1007/BF00034281.
[15] Sarrado C, Turon A, Costa J, Renart J. On the validity of linear elastic fracture mechanics methods to measure the fracture toughness of adhesive joints. Int J Solids Struct 2016;81:110–6. http://dx.doi.org/10.1016/j.ijsolstr.2015.11.016.
[16] Biel A, Stigh U. Comparison of J-integral methods to experimentally determine cohesive laws in shear for adhesives. Int J Adhes Adhes 2019;94:64–75. http://dx.doi.org/10.1016/j.ijadhadh.2019.04.014.
[17] Georgiou I, Hadavinia H, Ivankovic A, Kinloch AJ, Tropsa V, Williams JG. Cohesive zone models and the plastically deforming peel test. J Adhes 2003;79(3):239–65. http://dx.doi.org/10.1080/00218460309555.
[18] Kawashita L, Kinloch A, Moore D, Williams J. A critical investigation of the use of a mandrel peel method for the determination of adhesive fracture toughness of metal-polymer laminates. Eng Fract Mech 2006;73(16):2304–23. http://dx.doi.org/10.1016/j.engfracmech.2006.04.025.
[19] Kanninen MF. An augmented double cantilever beam model for stud propagation and arrest. 1973, p. 10.
[20] Stigh U, Alfredsson KS, Biel A. Measurement of cohesive laws and related problems. In: Mechanics of solids, structures and fluids. vol. 11, Florida, USA: ASMEDC, Lake Buena Vista; 2009, p. 293–8. http://dx.doi.org/10.1115/IMECE2009-10474.
[21] Blondeau C, Pappas G, Botsis J. Influence of ply-angle on fracture in antisymmetric interfaces of CFRP laminates. Compos Struct 2019;216:464–76. http://dx.doi.org/10.1016/j.compstruct.2019.03.004.
[22] Sika. SikaPower®-1277, product data sheet. 2019.
[23] D30 Committee. Test method for mode I interlaminar fracture toughness of unidirectional fiber-reinforced polymer matrix composites. Tech. rep., ASTM International, http://dx.doi.org/10.1520/D5528-13.
[24] Sørensen BF. Cohesive law and notch sensitivity of adhesive joints. Acta Mater 2002;50(5):1053–61. http://dx.doi.org/10.1016/S1359-6454(01)00404-9.
[25] Walander T, Biel A, Stigh U. Temperature dependence of cohesive laws for an epoxy adhesive in Mode I and Mode II loading. Int J Fract 2013;183(2):203–21. http://dx.doi.org/10.1007/s10704-013-9887-3.
[26] Sarrado C, Turon A, Costa J, Renart J. An experimental analysis of the fracture behavior of composite bonded joints in terms of cohesive laws. Composites A 2016;90:234–42. http://dx.doi.org/10.1016/j.compositesa.2016.07.004.
[27] Sarrado C, Turon A, Renart J, Costa J. An experimental data reduction method for the Mixed Mode Bending test based on the J-integral approach. Compos Sci Technol 2015;117:85–91. http://dx.doi.org/10.1016/j.compscitech.2015.05.021.
[28] Herráez M, Pichler N, Pappas G, Blondeau C, Botsis J. Experiments and numerical modelling on angle-ply laminates under remote mode II loading. Composites A 2020;134:105886. http://dx.doi.org/10.1016/j.compositesa.2020.105886.
[29] Pichler N, Herráez M, Botsis J. Mixed-mode fracture response of anti-symmetric laminates: Experiments and modelling. Composites B 2020;197:108089. http://dx.doi.org/10.1016/j.compositesb.2020.108089.
[30] Beer FP, editor. Mechanics of materials. 6th ed. New York: McGraw-Hill; 2011.
[31] Yu TX, Zhang LC. Plastic bending: theory and applications. WORLD SCIENTIFIC; 1996, http://dx.doi.org/10.1142/2754.
[32] Virtanen P, Gommers R, Oliphant TE, Haberland M, Reddy T, Cournapeau D, et al. SciPy 1.0 contributors, SciPy 1.0: Fundamental algorithms for scientific computing in python. Nature Methods 2020;17:261–72. http://dx.doi.org/10.1038/s41592-019-0686-2.
[33] Kierzenka J, Shampine LF. A BVP solver based on residual control and the Maltab PSE. ACM Trans Math Software 2001;27(3):299–316. http://dx.doi.org/10.1145/502800.502801.
[34] Blackman BRK, Kinloch AJ, Paraschi M. The effect of the substrate material on the value of the adhesive fracture energy, Gc: further considerations. J Mater Sci Lett 2001;20(3):265–7. http://dx.doi.org/10.1023/A:1006705808948.
[35] Lopes Fernandes R, Teixeira de Freitas S, Budzik MK, Poulis JA, Benedictus R. Role of adherend material on the fracture of bi-material composite bonded joints. Compos Struct 2020;252:112643. http://dx.doi.org/10.1016/j.compstruct.2020.112643.
[36] Abdel Monsef S, Pérez-Galmés M, Renart J, Turon A, Maimí P. The influence of mode II test configuration on the cohesive law of bonded joints. Compos Struct 2020;234:111689. http://dx.doi.org/10.1016/j.compstruct.2019.111689.

[37] Wang W, Hosseini A, Ghafoori E. Experimental study on Fe-SMA-to-steel adhesively bonded interfaces using DIC. Eng Fract Mech 2021;244:107553. http://dx.doi.org/10.1016/j.engfracmech.2021.107553.
[38] Smith M. ABAQUS/standard user's manual, version 6.14. 2017.
[39] Williams J, Hadavinia H. Analytical solutions for cohesive zone models. J Mech Phys Solids 2002;50(4):809–25. http://dx.doi.org/10.1016/S0022-5096(01)00095-3.
[40] Plaut RH, Ritchie JL. Analytical solutions for peeling using beam-on-foundation model and cohesive zone. J Adhes 2004;80(4):313–31. http://dx.doi.org/10.1080/00218460490445832.
[41] Škec L, Alfano G, Jelenić G. Complete analytical solutions for double cantilever beam specimens with bi-linear quasi-brittle and brittle interfaces. Int J Fract 2019;215(1–2):1–37. http://dx.doi.org/10.1007/s10704-018-0324-5.
[42] Sekiguchi Y, Hayashi A, Sato C. Analytical determination of adhesive layer deformation for adhesively bonded double cantilever beam test considering elastic–plastic deformation. J Adhes 2020;96(7):647–64. http://dx.doi.org/10.1080/00218464.2018.1489799.
[43] Majano-Majano A, Lara-Bocanegra A, Pereira F, Xavier J, Morais J, de Moura M. Direct and inverse cohesive law identification of hardwood bonded joints with 1C-PUR adhesive using DCB test. Compos Struct 2023;117013. http://dx.doi.org/10.1016/j.compstruct.2023.117013.